Nonlinear Analysis of a 10-Story Building Shake Table Specimen with Mass Timber Rocking Walls

Sarah Wichman, A.M.ASCE[1]; Jeffrey W. Berman, A.M.ASCE[2]; Reid B. Zimmerman, M.ASCE[3]; and Shiling Pei, F.ASCE[4]

Abstract: Mass timber buildings are becoming increasingly popular in the United States and around the world as they offer benefits such as fast construction, a desirable aesthetic, and the use of a sustainable building material. Using a post-tensioned mass timber rocking wall lateral system makes the construction of fully timber-based tall buildings in high seismic areas feasible and can help buildings achieve seismic performance objectives beyond those required by current building codes. This paper presents the three-dimensional nonlinear OpenSees numerical model used for the performance-based design of a full-scale 10-story mass timber building with a post-tensioned mass timber rocking wall lateral system for dynamic shake table testing. Model results demonstrate that the behavior of the building meets performance targets utilized in design processes similar to what is required for tall buildings in urban areas in the United States. The numerical model's ability to replicate shake table test results provides confidence that future projects which aim to use post-tensioned mass timber rocking walls in tall buildings can use this robust modeling method to reliably predict seismic performance. **DOI: 10.1061/JSENDH.STENG-15010.**
This work is made available under the terms of the Creative Commons Attribution 4.0 International license, https://creativecommons.org/licenses/by/4.0/.

Author keywords: Mass timber; Rocking walls; Shake table testing; Seismic performance; Numerical modeling.

This work is made available under the terms of the Creative Commons Attribution 4.0 International license.

Introduction and Background

Mass timber building construction is increasing worldwide thanks to recent advances in mass timber materials and growing market appreciation of the sustainability benefits. At the same time, there is a need to build midrise and high-rise buildings to aid in increased housing demands. These market forces have combined to enable many midrise and high-rise building projects that utilize mass timber components for the gravity force-resisting system. Such projects include the 19-story Ascent MKE building located in Milwaukee, WI, USA, the 18-story Brock Commons building in Vancouver, BC, Canada, and the 8-story Carbon12 building in Portland, OR, USA.

In high seismic zones, mass timber gravity framing is typically coupled with ductile lateral force-resisting systems of either steel or reinforced concrete components, such as steel buckling-restrained braced frames (Carbon12) or reinforced concrete shear walls (Brock Commons). Mass timber lateral force-resisting systems have architectural and sustainability appeal while also removing the need for multiple trades on site, which can further speed construction. Post-tensioned (PT) mass timber rocking walls provide an opportunity to couple mass timber construction with resilient seismic performance (with damage limited to easily repairable elements for all but the largest seismic intensities). Mass timber rocking walls have been designed and implemented as the primary lateral force-resisting system for low-rise buildings such as Peavy Hall at Oregon State University, Corvallis, OR, USA, among other examples in New Zealand.

The PT mass timber rocking wall concept builds on the successful development of PT precast concrete rocking wall systems in the 1990s, largely through the Precast Seismic Structural Systems (PRESSS) program (Priestley 1991). That program included large-scale experiments and the development of design recommendations for precast concrete rocking walls (Kurama et al. 1999; Pampanin et al. 2001). Research by Palermo et al. (2006) extended the PT rocking wall concept to mass timber panels, specifically laminated veneer lumber (LVL), and demonstrated with quasi-static testing that the system can achieve ductile behavior and good energy dissipation when coupled with steel yielding devices. Iqbal et al. (2015) extended that work to test two parallel wall panels with U-shaped flexural plates (UFPs), developed by Kelly et al. (1972) and studied by Baird et al. (2014), between them to serve as the energy dissipation system. Ganey et al. (2017) conducted similar tests on cross-laminated timber (CLT) PT rocking walls, and they and Akbas et al. (2017) used the experiments to develop a set of idealized limit states that ranged from an effective linear limit to crushing of the CLT in the compression zone for use in design. More recently, Pei et al. (2019) tested a two-story mass timber building with PT mass timber rocking walls on a shake table for earthquakes representing a range of different hazard levels. Fig. 1 shows a schematic that is representative of the PT mass timber rocking walls tested in recent history and explored in this paper. The stress–strain curve is shown generically for the compression zone of the mass timber panel. The transition points correspond to the idealized limit states from Ganey et al. (2017) that are identified schematically on the base shear versus base rotation hysteresis in Fig. 2. Finally, Brown et al. (2021) extended the concept to quasi-static tests of rocking C-shape CLT core walls.

[1]Structural Designer, KPFF Consulting Engineers, Seattle, WA 98101 (corresponding author). ORCID: https://orcid.org/0000-0003-0393-379X. Email: sarah.wichman@kpff.com

[2]Professor, Dept. of Civil and Environmental Engineering, Univ. of Washington, Seattle, WA 98195.

[3]Technical Director, KPFF Consulting Engineers, Portland, OR 97204.

[4]Associate Professor, Dept. of Civil and Environmental Engineering, Colorado School of Mines, Golden, CO 80401.

Note. This manuscript was submitted on January 28, 2025; approved on May 13, 2025; published online on August 23, 2025. Discussion period open until January 23, 2026; separate discussions must be submitted for individual papers. This paper is part of the ***Journal of Structural Engineering***, © ASCE, ISSN 0733-9445.

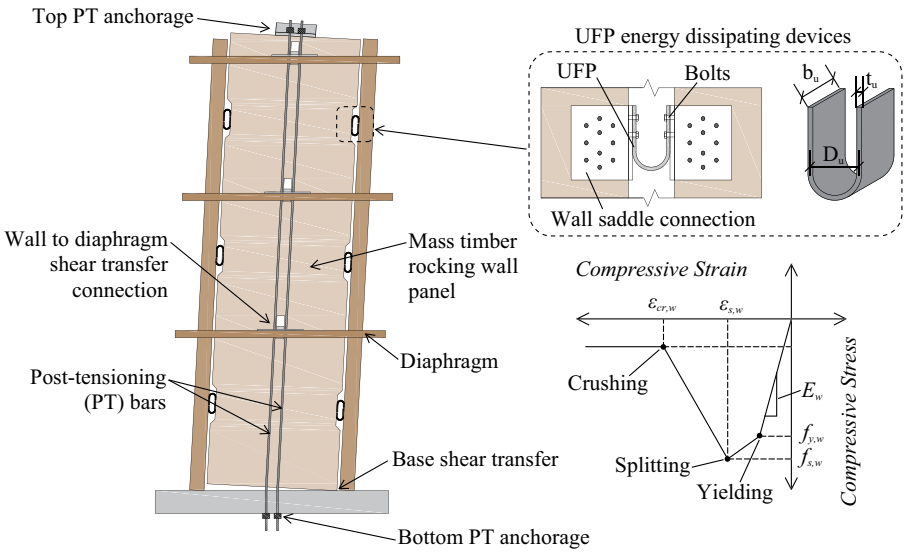

Fig. 1. PT rocking wall schematic.

Numerical modeling has made use of enhanced understanding provided by the large-scale experiments in the references above. Again, building on concepts originally developed for precast concrete systems, the common method for representing the rocking behavior of these walls is to use a series of springs at the rocking interface that distribute the nonlinear compressive timber behavior and allow uplift, denoted the distributed multispring model in the literature. Spieth et al. (2004) applied this nonlinear modeling method to PT precast concrete walls, and Palermo et al. (2005) extended its application to other PT precast concrete systems.

Sarti (2015) implemented the multispring model in OpenSees (McKenna et al. 2010) to model PT LVL rocking walls. The study examined three different shear wall configurations: (1) a single rocking panel with energy dissipation provided through yielding steel bars at the wall base, (2) paired rocking wall panels with energy dissipation provided by UFPs between the panels, and (3) a column-rocking wall system where a single panel was placed between two bounding columns with UFPs at the interface between the wall panel and the columns. The behavior of the springs at the rocking interface simulated the compressive response of the timber and was tension-only to allow uplift. Sarti (2015) found good agreement between the model and various experimental results. Similarly, Ganey (2015) developed a multispring model and simulated the tests summarized in Ganey et al. (2017) on CLT rocking walls. Again, good agreement was found between the experiments and nonlinear modeling for both single-panel rocking walls and paired walls with UFPs. Kovacs (2016) extended the multispring numerical model by using a Winkler spring analogy based on work by Newcombe et al. (2008). In all multispring models, the effective length for translating mass timber stress–strain response to spring force-displacement response is a key consideration. Newcombe (2015) developed an empirical relationship between this effective length and the neutral axis location at the base of the wall as rocking occurs. However, because the neutral axis location is not directly observed in analyses, it would have to be calculated at each time step during an analysis. Therefore, nonlinear modeling studies such as Kovacs (2016) have used a constant neutral axis location taken at the peak expected roof drift.

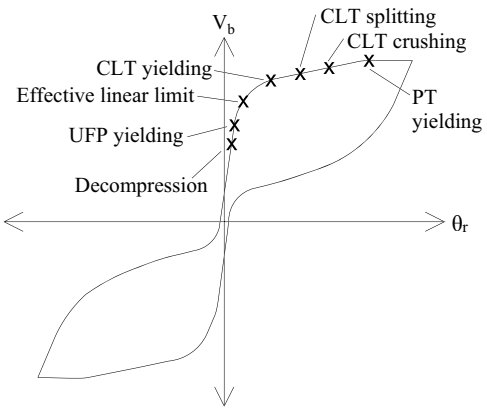

Fig. 2. Schematic hysteretic behavior of PT mass timber rocking walls with performance points indicated. (Reprinted from Ganey et al. 2017, © ASCE.)

Wichman et al. (2022) and Wichman (2018) used the multispring model to simulate the shake table testing response of two-story paired mass timber rocking walls from Pei et al. (2019). The modeling method was shown to compare well with the experimental results when the impact of foundation flexibility unique to this test was considered. The models were then used to simulate the response of the test specimen with the impacts of foundation flexibility removed and demonstrated that the specimen would have met performance objectives seeking to limit damage and provide recentering for all hazard levels below the risk-targeted maximum considered earthquake (MCE_R).

The research presented here is part of the Natural Hazards Engineering Research Infrastructure (NHERI) TallWood project (Pei et al. 2024b), which explores using PT mass timber rocking walls in midrise and taller mass timber buildings. The NHERI TallWood project recently completed seismic testing of a 10-story building, with PT mass timber rocking walls as the primary lateral force-resisting system, on the NHERI Large-Scale High Performance Outdoor Shake Table (LHPOST) at the University of California, San Diego. This paper presents the nonlinear model used to design the building and then later to compare with and help interpret the test results. The model utilizes an extension of the multispring model for representing the nonlinear response of tall PT mass timber rocking walls, with modifications to represent wall

This work is made available under the terms of the Creative Commons Attribution 4.0 International license.

rocking in both in-plane and out-of-plane directions. The model demonstrates the behavior of the building meets performance targets utilized in a design process similar to what is required for the design of tall buildings in urban US areas, utilizing the recommendations of the Los Angeles Tall Buildings Structural Design Council (LATBSDC) alternative procedure (LATBSDC 2014; Zimmerman and McDonnell 2018b), the Pacific Earthquake Engineering Research Center Tall Buildings Initiative Guidelines (PEER 2017), and ASCE 7-16 (ASCE 2016) Chapter 16. The numerical model prediction is then compared to the shake table test behavior.

Summary of the 10-Story Test Specimen

The performance of PT mass timber rocking walls in tall buildings was tested experimentally in a full-scale 10-story building shake table test at the NHERI LHPOST facilities in 2023. Fig. 3(a) shows a photo of the test. As shown in Fig. 3(b) elevations, the first story is 3.96 m and all other stories are 3.35 m, resulting in a roof elevation of 34.1 m. The walls are balloon-framed and extend 0.76 m above the roof. Fig. 3(c) shows a typical 9.75 m by 10.5 m floor plan. Exact details varied floor to floor, but geometry and general structural layout remained the same. The lateral force-resisting system consists of PT mass timber rocking walls with two lines of resistance in each direction. The walls are CLT in the east-west direction and mass plywood panel (MPP) in the north-south direction to study the performance of both materials. Each wall is PT with four external threaded rods that run the full height and are positioned near the center of each panel. At the base of the walls, a shear key detail was designed for shear force transfer into the foundation. A grid of steel and concrete foundation elements was fixed to the shake table and served as the support for the structure.

The gravity framing system consists of LVL gravity columns and beams that, in conjunction with the boundary columns, support all gravity load apart from the wall panel self-weight. Gravity system members were designed in accordance with the National Design Standard for Wood Construction (AWC 2018) for a two-hour fire rating. Beams, gravity columns, and boundary columns were 311 mm by 302 mm, 311 mm by 302 mm, and 445 mm by 302 mm, respectively. Gravity columns were orientated for strong axis bending in the east-west direction, and all boundary columns are orientated so their strong axis of bending is perpendicular to the strong axis bending of their corresponding wall. Gravity connections were designed and manufactured by Simpson Strong-Tie. Design calculations for the gravity members and details relating to the connections can be found in Busch et al. (2022).

Diaphragm spans were short, and thus, diaphragms were assumed rigid for the design of the lateral force-resisting system and nonlinear numerical modeling of the building. Though not the subject of this paper, CLT diaphragm design and numerical modeling of semirigid CLT diaphragms can be found elsewhere (WoodWorks 2023; Rodrigues et al. 2024; Barbosa et al. 2021). Floor diaphragm materials varied floor to floor, including sheathed and nonsheathed designs. More information regarding the different diaphragm systems can be found in Huang (2023), and a discussion on their response can be found in Wright (2023).

The specimen was designed to meet seismic demands computed per ASCE 7-16 for Site Class C in the Capitol Hill neighborhood of Seattle, WA, USA. A response modification coefficient, R, of 6, a seismic importance factor, I_e, of 1.0, and an approximate period calculated per ASCE 7-16 were used to compute the equivalent lateral force demands used in design. The design spectral acceleration parameters at short periods, S_{DS}, and at a period of 1 second, S_{D1}, were 1.102 g and 0.48 g, respectively. Note that seismic demands differ with ASCE 7-22 code adoption; however, the design procedure and resulting design will not change significantly.

The test specimen also included nonstructural elements such as stairs, interior partition walls, and exterior cladding at select stories. The walls were designed such that the contribution of these components to the overall strength and stiffness of the structure was negligible. Thus, the details, design, and performance of these components are omitted. More details of the building and the test program can be found in Pei et al. (2024b).

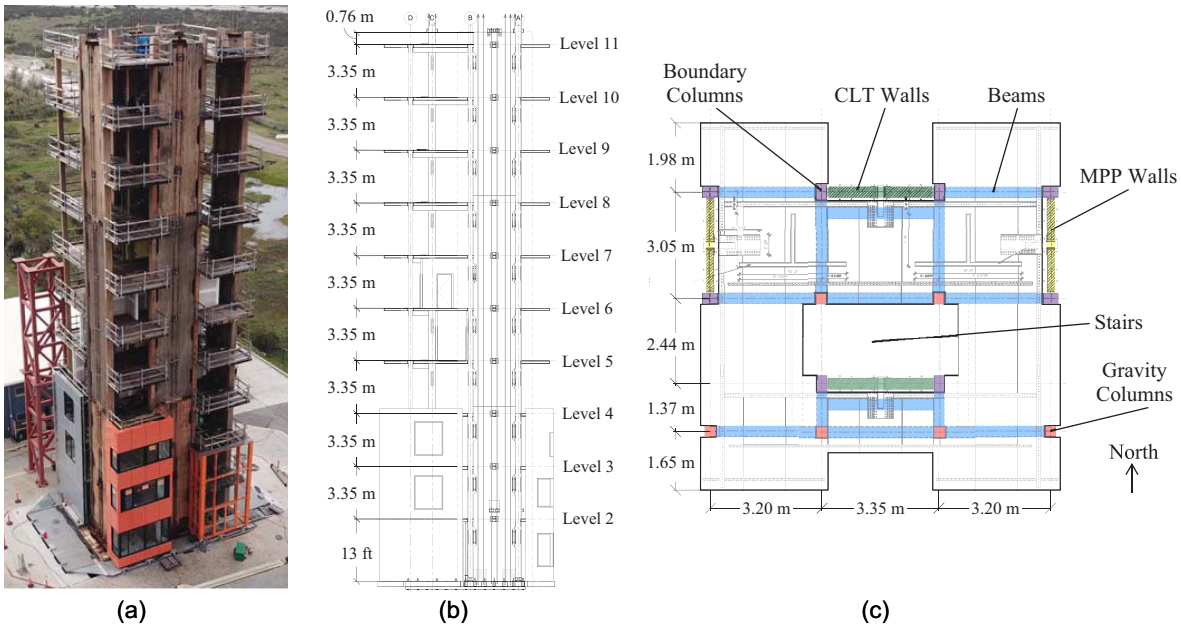

Fig. 3. Ten-story test building specimen: (a) photo of completed building; (b) schematic elevation view; and (c) schematic of typical structural floor plan.

J. Struct. Eng., 2025, 151(11): 04025180

This work is made available under the terms of the Creative Commons Attribution 4.0 International license.

Rocking Wall Lateral System

While research in mass timber lateral force-resisting systems is extensive, there is currently no prescriptive design method for this system in the US building code and referenced standards. Thus, performance-based design (PBD) methodologies were used for the 10-story lateral force-resisting system. The preliminary design of the walls was completed based on the prescriptive seismic design procedure for PT mass timber rocking walls proposed by Busch et al. (2022). The design was then finalized by further studying the calculated response using nonlinear response history analysis, and the predicted performance was checked using a series of global criteria and deformation- and force-controlled action limits at the MCE_R. The OpenSees model presented in this paper was used for design. A detailed discussion on the design can be found in Wichman (2023).

CLT and MPP Rocking Walls

Characterization of the compression behavior of mass timber panels at the rocking interface is crucial for design and nonlinear modeling. However, to date, there is no universally accepted compression constitutive relationship for mass timber panel material. In many studies, elastic-perfectly plastic material properties have been assumed to represent CLT behavior with strain limits (Ganey et al. 2017). However, a more complete nonlinear compression model was needed here to capture potential crushing at the base of the wall panels. Fig. 1 shows the assumed CLT and MPP compressive behavior used in this research. As shown, the compressive behavior is approximated as elastic, with modulus, E_w, until the yield stress, $f_{y,w}$, is reached. After yielding, softening is assumed until splitting begins at the splitting stress and strain, $f_{s,w}$ and $\epsilon_{s,w}$, respectively. In this research, a zero strain-hardening plateau was assumed between yielding and splitting for CLT. After splitting, the strength is assumed to deteriorate until crushing occurs at approximately 15% of the yield stress at the crushing strain, $\epsilon_{cr,w}$. This model was taken directly from Wichman (2023) and is developed based on test data from Soti et al. (2021).

The two CLT rocking walls were custom 9-ply panels from Smartlam with machine stress-rated lumber, grade 2400-2.0E in the major strength direction and Southern Pine, No. 1, visually grade lumber in the minor strength direction (AWC 2018). The two MPP rocking walls were 229 mm-thick Grade F16 panels from Freres Lumber (APA 2021). The width, b_w, length, L_w, and height, h_w, of the panels are summarized in Table 1. Table 1 also shows the assumed modeling material properties, including E_w, shear modulus, G_w, and the necessary stress and strain values to define the compressive behavior in Fig. 1. Note, E_w, G_w, $f_{y,w}$, and $F_{s,w}$ are reported for gross area.

Post-Tensioning Bars

The PT rods were Simpson Strong-Tie ATS high-strength, fully threaded rods (with elastic modulus, E_{pt}, of 2.0×10^5 MPa, and yield stress, $f_{y,pt}$, of 724 MPa) spanning continuously the full height of the walls. The lower portion of the bars was larger than the upper portion because they were also used for temporary lateral resistance during construction. The first one and a half stories were 51 mm diameter bars (length of bar, L_{pt} of 0.46 m and a net tensile area, $A_{net,pt}$ of 1613 mm^2). The remainder of the building height used 32 mm diameter bars (L_{pt} of 2.45 m and $A_{net,pt}$ of 625 mm^2). Four bars were placed at each wall with each bar PT to an initial force, $T_{o,pt}$, of 222 kN, equivalent to 21% and 55% of the yield force for the lower and upper bars, respectively.

UFP Energy Dissipating Devices

At every story, a UFP assembly existed on either side of each rocking wall, between the rocking wall edges and the boundary columns. The bottom three stories had larger UFPs with two UFPs per location, and the upper seven stories had smaller UFPs with only one UFP per location. The denser UFP layout aided in lateral resistance during construction. As shown in Fig. 4(a), the UFPs were anchored to the timber using an embedded plate connection with steel dowels. The UFPs connect to the embedded knife plate connections using bolts. All UFPs were made of A572 Grade 50 Steel (with elastic modulus, E_{ufp}, and yield stress, $f_{y,ufp}$). Table 2 summarizes UFP properties.

Wall-to-Diaphragm Shear Key and Wall Out-of-Plane Bracing Connections

The rocking walls connected to the diaphragms using the vertically slotted shear key connection shown in Fig. 4(b). A rounded cantilevered steel shear key (with an elastic modulus, E_{key}, of 2.010^5 MPa×, width, w_{key}, of 51 mm, and thickness, t_{key}, of 241 mm) is inserted into a vertically slotted hole in the walls, creating a slotted pin connection that transfers horizontal shear forces and allow for rotation and vertical movement from wall uplift, without transferring moment or vertical reaction. For this test, the vertically slotted hole was lined with PTFE to reduce friction. The concept for this connection comes from the permitted Framework building (Zimmerman and McDonnell 2018a) in Portland, Oregon, USA. A nearly identical connection performed successfully in the NHERI TallWood 2-story test (Pei et al. 2019). A wing plate system transferred force from the shear key to the diaphragm. Shear key design was consistent at all locations; however, the wing plate designs varied to accommodate different diaphragm splice locations and varied on sheathed diaphragms to properly engage the sheathing. The shear keys spanned a length, L_{key}, of 178 mm from the center of the wall to the edge of the wing plate, shown in Fig. 4(b).

Out-of-plane wall braces were installed to prevent wall compression buckling. A unique design that accommodated both the wall rotation and uplift at the diaphragms and could work for both the interior and exterior wall configurations was designed and manufactured by Simpson Strong-Tie. The resulting connection is shown in Fig. 4(b). On each wall face, at each story, two out-of-plane brace connections are installed at a distance d_{oop} of 2.51 m and 2.48 m for the CLT and MPP walls, respectively. Each out-of-plane brace connection has two vertically orientated steel legs (elastic modulus, E_{oop}, of 2.0×10^5 MPa, height, h_{oop}, of 76 mm, thickness, t_{oop}, of 10 mm, and spanning length, L_{oop}, from center of bolt hole to face of wing plate of 348 mm) that are anchored to the diaphragm with a small wing plate and then span to vertically slotted steel pin connections mounted to the walls.

Table 1. CLT and MPP wall panel dimensions and modeling property parameters (Wichman 2023)

Wall	b_w (m)	L_w (m)	h_w (m)	E_w (MPa)	G_w (MPa)	$f_{y,w}$ (MPa)	$f_{s,w}$ (MPa)	$\epsilon_{s,w}$ (m/m)	$\epsilon_{cr,w}$ (m/m)
CLT	0.31	2.97	34.9	7824	552	18	18	0.0079	0.0398
MPP	0.23	2.67	34.9	13817	862	33	41	0.0061	0.0276

This work is made available under the terms of the Creative Commons Attribution 4.0 International license.

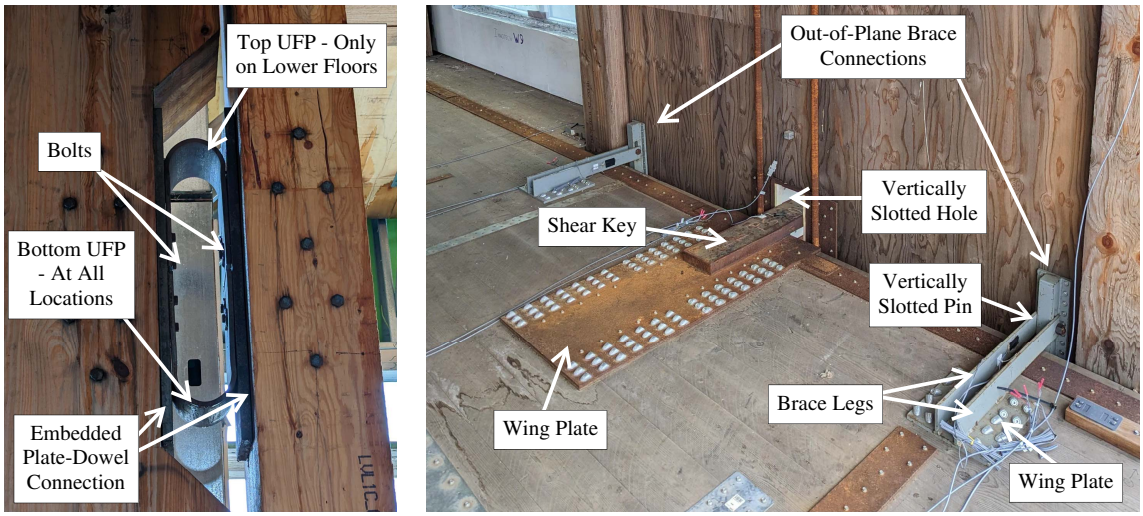

(a) (b)

Fig. 4. 10-story building details for the: (a) UFP connections; and (b) the wall-to-diaphragm shear key connections and out-of-plane brace connections.

The legs are connected to the vertically slotted hole using a bolt that was hand-tightened such that it was free to move vertically in the slot during wall uplift.

3D Nonlinear Numerical Model of the 10-Story Test Specimen

The three-dimensional (3D) nonlinear numerical model was developed using OpenSees and built upon two-dimensional (2D) modeling techniques presented in Ganey (2015) and Wichman et al. (2022) that validated the techniques using cyclic and dynamic loading tests, respectively. The primary use of this model was to design and study the behavior of the PT mass timber rocking walls and predict overall building performance. By design, gravity elements and nonstructural elements (including the stair system, interior partition walls, and exterior walls) contribute little to the overall building behavior, so the model does not include stiffness contributions from these elements.

Simulations in this study used Rayleigh damping models with the damping matrix proportional to the current stiffness matrix. The first and second Rayleigh damping coefficients were calculated using damping ratios of 0.05 and 0.06 for periods of 3.0 s and 0.12 s, respectively. While the first mode periods from modal analysis range from 1.7 s to 1.2 s, a period of 3.0 s was used for calculating the first mode Rayleigh damping coefficient to target the base rocking period, not the elastic first mode from modal analysis, which represents a fixed-based cantilever mode. The 0.12-second period used for calculating the second Rayleigh damping coefficient is representative of the third torsional mode, which is less than the period at which 90% mass participation occurs. A larger damping ratio was used for the second Rayleigh mode to capture the larger damping in the higher modes.

Table 2. UFP dimensions and material properties

Location	UFPs per wall	b_u (mm)[a]	t_u (mm)[a]	D_u (mm)[a]	E_{ufp} (MPa)	$f_{y,ufp}$ (MPa)
Lower	12	8	13	159	2.0×10^5	345
Upper	14	8	10	162	2.0×10^5	345

[a]See Fig. 1 for definitions of b_u, t_u, and D_u.

Rocking Wall Modeling

A schematic of the PT rocking wall OpenSees model is shown in Fig. 5. In mass timber rocking wall systems, the design intent is for the walls to remain elastic up their full height. All inelastic behavior occurs at the wall base through uplift and compressive deformations. The elastic portion of the wall is modeled using a series of force-based beam-column elements with rectangular fiber cross sections. The fiber cross sections are equivalent to the size of the wall panels (b_w by L_w) and consist of 348 fibers (58 by 6 patch) for the CLT walls and 208 fibers (52 by 4 patch) for the MPP walls. An elastic material model, with stiffness equal to the effective elastic modulus, E_w, was assigned to the wall fiber section to model flexural stiffness. Shear deformations were included by using the section aggregator command in OpenSees. An elastic material model with slope equal to $G_w k_{sf} A_w$ was used for shear flexibility, where G_w is the effective shear modulus, k_{sf} is the shear shape factor equal to 5/6 for the rectangular section, and A_w is the cross-sectional area of the wall (equal to $b_w L_w$). This material was then aggregated to the elastic fiber section in both in-plane shear directions. Reference Table 1 for the CLT and MPP wall model input parameters.

The inelastic compressive deformation of the wall base and the rocking behavior were modeled using a multispring contact element, which has been used previously in 2D models. For this newly developed 3D multispring contact element developed for this model, vertically orientated zero-length springs were distributed along the length of the wall base and through the thickness using a Lobatto integration method in both directions. This results in a higher concentration of springs at the rocking corners along both horizontal axes. The distribution consisted of 30 springs along the length of the wall base and seven rows of springs through the thickness. Fig. 5 includes a simplified illustration of this multispring element. The top of each spring connected to the base of the wall element using a horizontal rigid element, and each base was fixed. To transfer shear at the wall base, the tops of the zero-length springs in the four corners of the multispring element were restrained in both horizontal directions. Each corner of the wall panel base

This work is made available under the terms of the Creative Commons Attribution 4.0 International license.

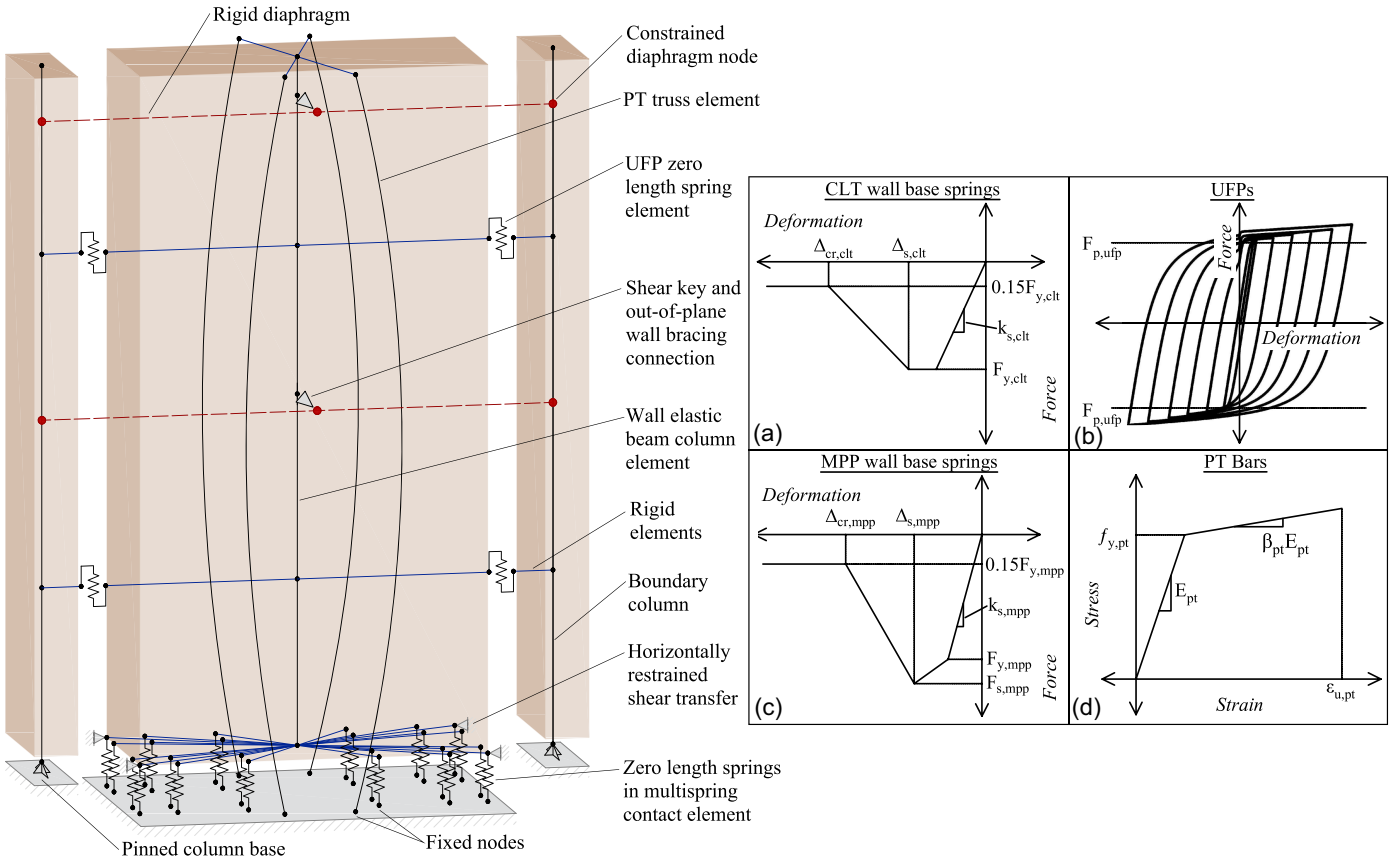

Fig. 5. Numerical model schematic of the PT rocking walls: (a) CLT wall base springs; (b) UFPs; (c) MPP wall base springs; and (d) PT bars.

was tapered by 51 mm to accommodate the shear transfer connection, so the length of the multispring element was 102 mm shorter than the wall length.

Fig. 1 shows the compressive stress–strain behavior that this multispring element captures. An assumed effective strain penetration zone length, l_p, was used to transform this stress–strain compression behavior to a force-deformation behavior needed for the zero-length springs [Figs. 5(a and b) for the CLT and MPP walls, respectively]. In this model, an effective strain penetration zone length of $2b_w$ was assumed in accordance with Akbas et al. (2017) and validated in Wichman et al. (2022). The effective strain penetration zone length was used in calculating an overall contact stiffness of the multispring element K_s, in accordance with Eq. (1). This stiffness was then proportionally scaled based on the Labatto weighted area to determine the stiffness of each zero-length spring, k_s. For each spring, the product of the panel yield stress, $f_{y,w}$, and the Labatto weighted area determined each yield strength, $F_{y,s}$. Using similar logic, the product of the respective strains, $\epsilon_{s,w}$ and $\epsilon_{cr,w}$, and the effective strain penetration zone length, l_p, determined the splitting deformation, Δ_s, and the crushing deformation, Δ_{cr}, respectively, for each zero-length spring. The compression-only portion of the constitutive model simulates base rocking and the hysteretic portion of the model simulates the compression crushing behavior of the panels

$$K_s = \frac{b_w L_w E_w}{l_p} \tag{1}$$

To counteract the increased axial flexibility of the wall resulting from the addition of the multispring element (i.e., due to "double-counting" of the axial flexibility over the effective strain penetration zone length by adding in the zero-length springs), a truss element spanning from the top of the wall panel to the top of the multispring element was added to increase the axial stiffness of the wall. The truss element had an elastic material model, with an elastic modulus equal to the wall, E_w, and an area, A_w^*, calculated as shown in Eq. (2)

$$A_w^* = b_w L_w \left(\frac{l_p}{h_w - l_p}\right) \tag{2}$$

The PT bars were modeled using corotational truss elements that connected a fixed node at the wall base to the end of a cantilevered rigid element at the top of the wall, representing the PT offset from the centerline of the wall. A tension-only bilinear hysteretic material model that allows for damage accumulation after yielding was used for the PT elements [Fig. 5(d)]. The initial post-tensioning of the PT elements was simulated by applying an initial strain wrapper in OpenSees. For simplicity in the model, the smaller diameter bars (upper bars) were assumed for the entire height of the wall. Because the length of the larger lower bars is short in comparison to the whole building, this approximation did not have a significant effect on the overall performance of the model. A higher initial PT force, $T_{o,pt}^*$, was applied to the bars to correct for the initial elastic wall shortening from the initial PT force and ensured the target PT force, $T_{o,pt}$, was achieved. This larger force is calculated using Eq. (3), where k_w is the elastic stiffness of the wall calculated as $b_w L_w E_w / h_w$ and k_{pt} is the elastic stiffness of the PT bars calculated as $A_{pt} E_{pt} / h_w$

J. Struct. Eng., 2025, 151(11): 04025180

This work is made available under the terms of the Creative Commons Attribution 4.0 International license.

$$T^*_{o,pt} = T_{o,pt}\left(\frac{k_{pt}}{k_w} + 1\right) \tag{3}$$

The boundary and gravity columns were modeled using continuous elastic beam-column elements with pinned bases. An elastic and shear modulus of 12.4 GPa and 241 MPa, respectively, was assumed for the column material model. Because lateral contributions from the gravity connections were designed to be small, they were omitted in this model.

Each UFP was modeled as a zero-length spring located at the midpoint between the wall edge and the respective boundary column. Note that the UFP wall cutouts are not accounted for in the location offset but are not expected to affect results significantly. Based on recommendations in Ganey (2015), a Giuffrè–Menegotto–Pinto steel material model with isotropic strain-hardening is assigned to the vertical direction of the zero-length springs to model the UFP behavior. The yield force and stiffness are calculated in accordance with equations from Kelly et al. (1972) and Baird et al. (2014). The assigned stiffness in all remaining degrees of freedom (DOFs) is near-zero. In the model, the UFP locations were assumed to be at the midheight of every story.

Diaphragm-to-Wall Connection and Rigid Diaphragm Modeling

The diaphragm-to-wall shear key connection and the out-of-plane braces were modeled by adding a second node at each wall and floor intersection and connecting the two nodes with a zero-length spring. As shown in Fig. 6 and described below, different elastic stiffness values were applied to the different zero-length spring DOFs to model the flexibility from the shear key and the out-of-plane braces. The free end of the spring was incorporated into the rigid diaphragm model. The flexibility of the cantilevered shear key [Fig. 4(b)] was modeled by assigning an elastic material model to the horizontal in-plane wall translational DOF of the zero-length spring. The stiffness for this DOF, $k_{key,inplane}$, accounted for both flexural stiffness, $k^f_{key,inplane}$, and shear stiffness, $k^s_{key,inplane}$ [see Eqs. (4)–(6)]. The shear modulus of the shear key, G_{key}, was calculated using Poisson's ratio for steel. While shear contributions were included in the cantilevered flexibility of the shear key, they are not expected to affect the stiffness significantly. The zero-length spring had negligible stiffness in the vertical DOF to allow for vertical uplift of the rocking walls

$$k^f_{k,inplane} = \frac{3E_{key}(w^3_{key}t_{key}/12)}{L^3_{key}} \tag{4}$$

$$k^s_{key,inplane} = \frac{G_{key}w_{key}t_{key}}{L_{key}} \tag{5}$$

$$k_{key,inplane} = \frac{k^f_{key,inplane}k^s_{key,inplane}}{k^f_{key,inplane} + k^s_{key,inplane}} \tag{6}$$

Axial flexibility from the cantilevered out-of-plane brace legs [Fig. 4(b)] was modeled using the horizontal DOF of the zero-length spring that is perpendicular to the face of the walls. An elastic material model with stiffness, $k_{oop,axial}$, [calculated using Eq. (7)] was assigned to this DOF

$$k_{oop,axial} = \frac{t_{oop}h_{oop}E_{oop}}{L_{oop}} \times 4legs \tag{7}$$

The rotational stiffness from the two out-of-plane braces at each wall on each floor level [Fig. 4(b)] was modeled by assigning an elastic material model to the out-of-plane wall rotational DOF in the zero-length spring. Spring stiffness was calculated using Eq. (8). In this equation, the number of legs is divided by 2 because the full moment arm length, d_{oop}, was used rather than the moment arm to the centroid of the out-of-plane braces. The other two rotational DOFs for this zero-length spring were assigned negligible stiffness since neither the shear key nor out-of-plane braces provides restraint of movement in these directions. Note, this model does not account for flexibility of the screws which is likely significant, if not more so, than the steel. Thus, the stiffnesses are a conservative upper-bound approximation of the wall-to-diaphragm connections

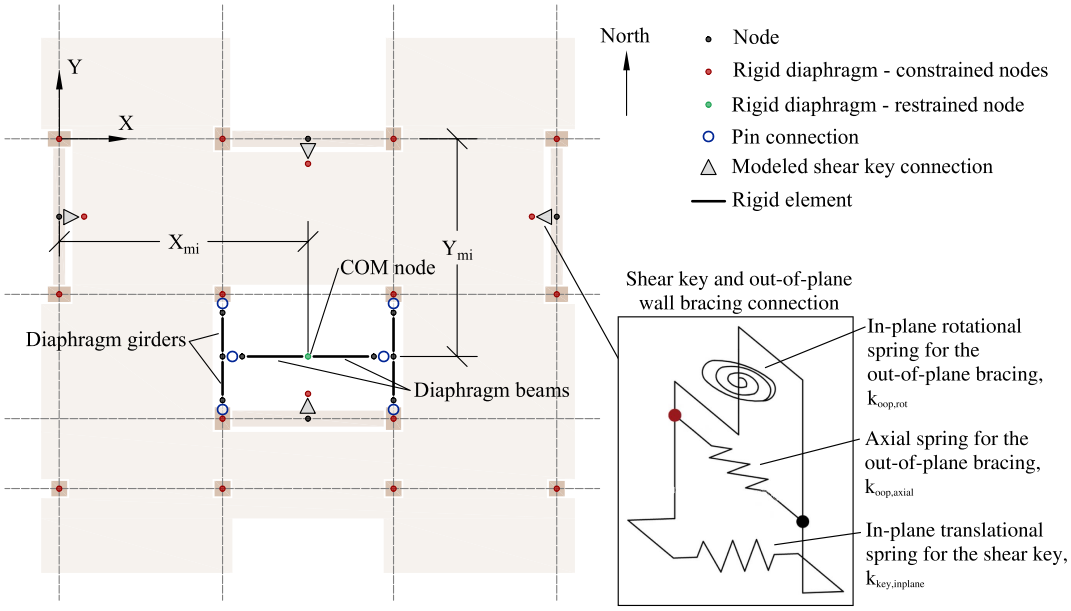

Fig. 6. OpenSees diaphragm model schematic.

J. Struct. Eng., 2025, 151(11): 04025180

This work is made available under the terms of the Creative Commons Attribution 4.0 International license.

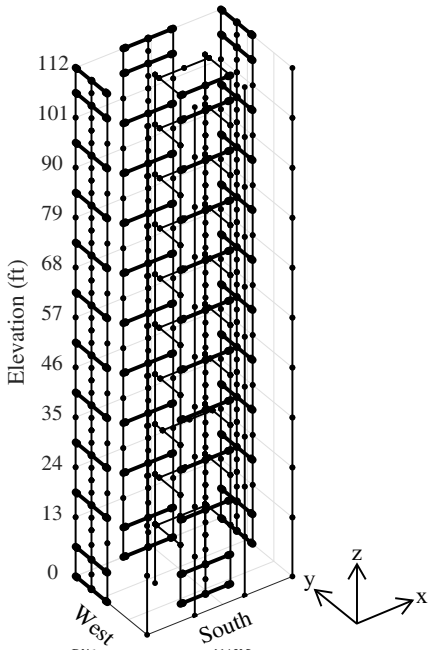

Fig. 7. Schematic of the full 10-story specimen OpenSees model.

$$k_{oop,rot} = \frac{t_{oop} h_{oop} E_{oop}}{L_{oop}} \times \frac{4legs}{2} \times d_{oop} \quad (8)$$

Because diaphragm spans are short, their flexibility is small relative to the lateral system. Thus, a rigid diaphragm was assumed at all levels. The rigid diaphragm model was implemented by adding a node at the calculated center of mass. The rigid diaphragm constraint command in OpenSees was utilized by assigning the center of mass node as the retained node. The constrained nodes were the four free end nodes of the diaphragm-to-wall shear transfer spring on each floor and the 14 column nodes on each floor. In OpenSees, the vertical direction was defined as the direction perpendicular to the rigid plane.

As shown in Fig. 6, an assembly of simply supported beams and girders was modeled to support the center of mass node. These added beams and girders are not representative of the real beams in the building but were added to vertically support the center of mass node. The beam and girder elements were modeled with elastic beam-column elements with a high modulus of elasticity to limit deformations. Fig. 7 shows a schematic of the full 10-story building OpenSees model. Note that Wright (2023) developed a numerical model for each of the diaphragm types and studied the vertical response of the systems during shake table testing.

Application of Seismic Mass and Gravity Loads

Approximations for building seismic mass and gravity loads were taken directly from Wichman (2023). The seismic mass of the wall panels and the mass of any significant lateral connections on the walls were distributed proportionally up the height of the wall panels. Table 3 shows the mass per floor, i, for the CLT, $m_{i,clt}$, and MPP, $m_{i,mpp}$. These masses were evenly distributed and assigned to nodes spaced at quarter points within each story. The mass was assigned to the two horizontal DOFs. The remainder of the building mass, m_i, and the corresponding approximate rotational moment of inertia, I_{oi}, were assigned to the diaphragm center of mass node on each floor. At this node, the mass was applied to the two horizontal DOFs, and the rotational moment of inertia was applied to the rotational DOF about the vertical axis. The centers of mass X_{mi} and Y_{mi} in the east-west and north-south directions, respectively, are measured from the center of the most north-west column in the floor plan [see Fig. 3(c)], where the positive x direction is east and the positive y direction is north. Values for the mass, rotational moments of inertia, and the location of the diaphragm center of mass node are shown in Table 3. For the gravity loading analysis, vertical loads equivalent to the seismic masses were applied to the structure. For the walls, equivalent gravity loads were applied, lumped at floor levels instead of at quarter points. The remaining gravity load was applied to the COM node.

Table 3. Summary of the 10-story building mass distribution per floor

Floor	$m_{i,clt}$ (Mg)	$m_{i,mpp}$ (Mg)	m_i (Mg)	I_{oi} (Mg m^2)	X_{mi} (m)	Y_{mi} (m)
2	2.93	2.15	24.42	6,586	4.79	−3.19
3	2.10	1.52	23.13	5,781	4.95	−3.45
4	3.28	2.51	22.80	4,549	5.01	−3.77
5	2.10	1.52	17.89	3,316	4.86	−3.55
6	2.10	1.52	17.61	3,254	4.86	−3.44
7	2.10	1.52	16.61	3,126	4.88	−3.54
8	3.28	2.51	18.46	3,581	4.88	−3.52
9	2.10	1.52	17.78	3,544	4.88	−3.50
10	2.10	1.52	17.65	3,542	4.88	−3.49
Roof	2.17	1.72	16.13	3,428	4.88	−3.44
Total	24.27	18.01	192.48	—	—	—

Ground Motion Subset for Model Validation

A comprehensive testing plan was developed to study the performance of the 10-story specimen (Pei et al. 2024b). Ground motion suites were selected and scaled to characterize the seismic hazard of the Seattle, WA, USA, design location at five hazard levels. The hazard levels were: 43-year return period, 225-year return period, 475-year return period, 975-year return period, and MCE_R. Target spectra for the first four hazard levels were defined using the geometric mean 5%-damped uniform hazard spectra (UHS) curves. The target spectrum for the MCE_R hazard level was defined as the probabilistic site-specific MCE_R, developed in accordance with ASCE 7-16 Chapter 21. For this paper, a subset of the testing plan was selected for comparison between analytical and experimental behavior.

At each hazard level, the full ground motion suite consisted of 11 bidirectional horizontal ground motions that most closely matched the target spectra. Three different types of earthquakes were used to characterize the unique seismic hazard in Seattle. The first type consisted of crustal earthquakes (CR) obtained from the NGA West-2 PEER Ground Motion Database (Ancheta et al. 2014). The second type consisted of interface earthquakes (IF) that occur at the boundary between tectonic plates in subduction zones. These motions were obtained from the Strong-motion Seismograph Networks KiK-net and K-NET database (NIED 2018). The third type consisted of intraslab (IS) earthquakes that occur within the subducting tectonic plate in subduction zones. These motions were obtained from the NGA-Subduction Flatfile data set (Mazzoni et al. 2021). Motions were scaled in accordance with ASCE 7-16 Chapter 16 utilizing amplitude scaling methods and a period range of 0.14 s to 3.4 s. This period range corresponds to a period that captures 90% mass participation and to two times the first mode period, respectively. While the ground motion scaling procedures in Chapter 16 of ASCE 7-16 are specified for the MCE_R hazard only, the same method was used at all hazard levels. A full list

This work is made available under the terms of the Creative Commons Attribution 4.0 International license.

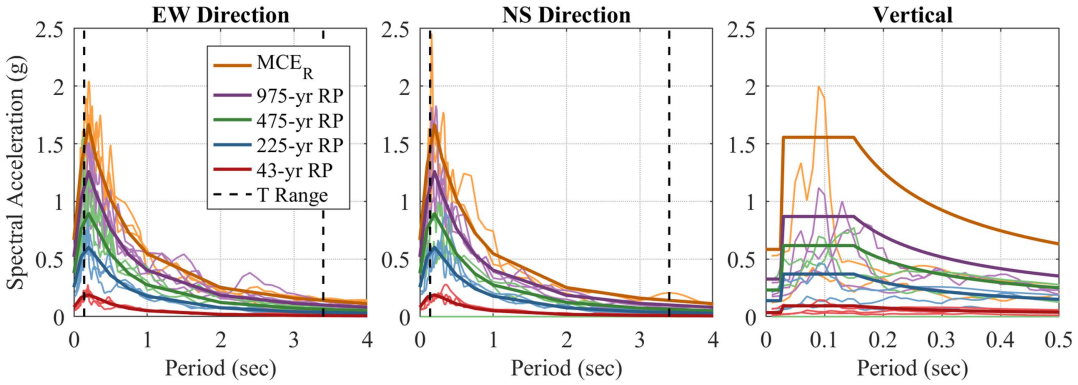

Fig. 8. Response spectra for the ground motions used in shake table testing.

of the ground motion suites generated at each hazard level can be found in Wichman (2023). The testing plan subset consisted primarily of one- and two-horizontal-component acceleration inputs, and some tests included vertical accelerations. Reference Wichman (2023) for the full testing plan. Fig. 8 shows the target response spectra for the ground motions tested on the shake table.

The subset of ground motion tests used for this paper is summarized in Table 4. Each test was assigned a unique test ID consisting of its respective hazard level, followed by a number. Table 4 also includes key details about each test including the earthquake source, name, year, motion name, and recording station. The motion identification number (MID) can be used to identify the corresponding motion in the published data set (Pei et al. 2024a). The component column in Table 4 indicates which component of the original ground motion recording was applied to the X (east-west) and Y (north-south) shake table direction.

The effective scale factors (SF) in Table 4 are the approximate SF that, if applied to the original input ground motion recording, would achieve the approximate motion executed by the shake table. This accounts for errors between the input and executed table motion. These SFs were calculated by dividing the executed shake table ground motion by the original ground motion recording and then averaged over the period range used for horizontal ground motion scaling. The period range used for the vertical components was 0.01 s to 0.1 s. For the horizontal components, the effective SF was generally close to the target SF. For the vertical components, the effective SF was consistently and significantly greater than the target SF, meaning the shake table did not replicate the vertical ground motion components as accurately as the horizontal components. For each test shown in Table 4, SFs were only calculated for directions in which a ground motion component was executed.

Comparison of Experimental and Numerical Results

In this section, the experimental and numerical results are compared to validate the presented nonlinear numerical modeling methodology. For this comparison, the true executed ground motion recordings from the shake table were input into the OpenSees model. Additionally, only the two horizontal ground motion components were used, as investigating vertical ground motion effects was outside the scope of the presented work.

Relative floor displacements from experimental and numerical results were compared. Experimental floor displacements were calculated using two methods. First, using filtered and double-integrated accelerometer recordings on each floor, where relative displacements are between each floor and the table. The second method used unfiltered story displacement recordings calculated from diagonal string potentiometers spanning between each floor in each direction. Interstory displacements were calculated using

Table 4. Subset of ground motion tests selected for numerical model validation

							Component		Effective SF		
Test ID	Source	EQ Name	Year	Motion Name	Station	MID	X	Y	X	Y	**Z**
43-03	IS	Ferndale	2001	subRSN2000905	1746	49	090	360	0.53	0.56	—
43-06	IF	Tohoku	2011	CHBH041103111446	CHBH04	52	NS2	EW2	0.24	0.25	—
43-09	CR	Niigata, Japan	2003	4213	NIG023	55	EW	NS	0.25	0.26	—
225-04	IS	Ferndale	2010	subRSN2000905	1746	59	090	360	1.68	1.85	—
225-07	IF	Tohoku	2011	CHBH041103111446	CHBH04	62	NS2	EW2	0.88	0.89	—
225-10	CR	Niigata, Japan	2004	4213	NIG023	68	EW	NS	0.85	0.84	—
475-04	CR	Chi-Chi	1999	3471	TCU075	46	E	N	4.97	4.50	—
475-12	IS	Ferndale	2010	subRSN2000905	1746	74	090	360	2.52	2.83	—
475-14	IF	Tohoku	2011	CHBH041103111446	CHBH04	76	EW2	—	1.25	—	—
975-03	CR	Northridge-01	1994	964	Compton—Castlegate St	79	270	000	3.85	4.40	—
975-04	IF	Tohoku	2011	CHBH041103111446	CHBH04	82	EW2	—	1.78	—	—
975-07	IS	Ferndale	2010	subRSN2000890	89486	85	090	360	3.46	3.69	—
975-10	IF	Tokachi	2003	HKD1270309260450	HKD127	91	NS	—	3.39	—	—
975-11	CR	Victoria, Mexico	1980	268	SAHOP Casa Flores	92	280	010	5.45	5.35	7.64
MCE$_R$-01	CR	Loma Prieta	1989	761	Fremont—Emerson Court	88	180	090	3.88	4.08	2.99
MCE$_R$-02	IS	Ferndale	2010	subRSN2000890	89486	90	090	360	4.72	4.99	3.08
MCE$_R$-03	IF	Tohoku	2011	CHBH041103111446	CHBH04	93	EW2	—	2.48	—	—

This work is made available under the terms of the Creative Commons Attribution 4.0 International license.

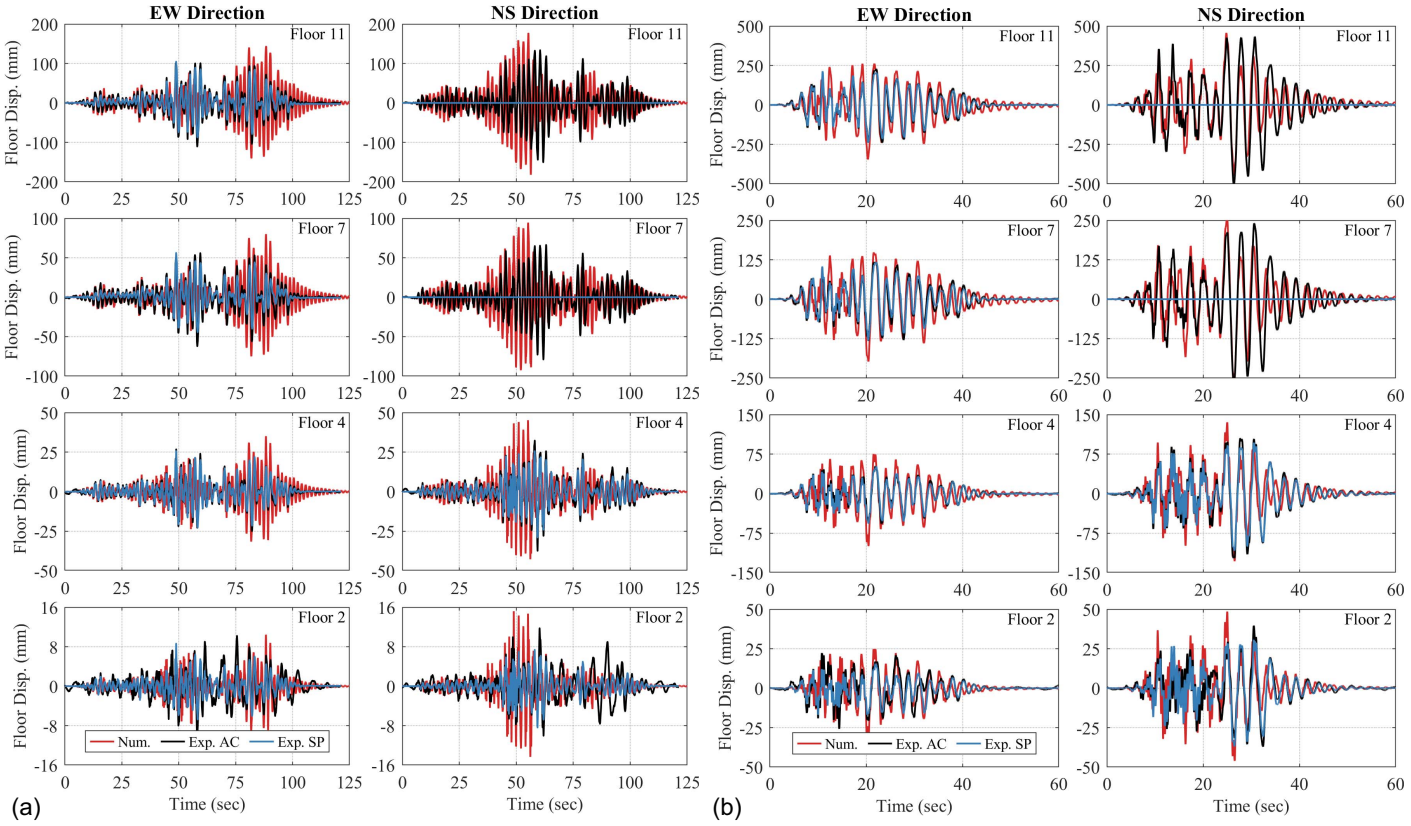

Fig. 9. Experimental and numerical floor displacement time history comparisons for test ID: (a) 225-07; and (b) MCE_R-01.

the change in length of the diagonal span to calculate the horizontal displacement component. With this calculation, negligible vertical diaphragm deformations between stories were assumed. Total floor displacements were calculated by summing the interstory displacements of all stories below. Note that floor displacements in the north-south direction using this method could only be calculated up to floor 4 because the diagonal string potentiometers were not present in the north-south direction on stories 4 and 5 due to interference with nonstructural walls.

Fig. 9 shows a comparison of experimental and numerical floor displacement results for test ID 225-07 and MCE_R-01. For conciseness, time history results are only shown for two ground motions and four floors. Similar trends were present on the other floors and in the other tests. The figure shows experimental results calculated using both methods.

Experimental results in Fig. 9 show that relative floor displacements calculated from the accelerometer data and the string potentiometer data match relatively well. For small floor displacements, like those shown for Floor 2 in Fig. 9(a) (i.e., a low intensity motion), the string potentiometer results are less than the accelerometer results. For the smaller ground motions, the accelerometer data are likely more representative of the true building response because the string potentiometers are measuring displacement over a very long distance, making any sag in the string more significant relative to the measurement.

Fig. 9 shows that numerical and experimental results match relatively well in terms of the displacement history shape in time as well as the peak floor displacement magnitude. These results show that the nonlinear model slightly overpredicts the response in the east-west direction and slightly underpredicts the response in the north-south direction. This discrepancy is likely due to contributions from the stairs and gravity system connections that are not accounted for in the numerical model, and though specifically designed to contribute little to the overall building response, they are judged to be more significant in the east-west direction. Note that the relative difference between experimental and numerical response appears to be greater for the smaller ground motion (i.e., the 225-year return period motion).

Peak floor displacement profile comparisons were also developed and are shown in Fig. 10 for test IDs 225-07 and MCE_R-01. In this figure, peak positive and peak negative responses are shown. In the north-south direction, peak values of experimental results using the displacement measurements are only shown for floors 1 through 4 due to the missing string potentiometers on floors 4 and 5. Overall, this figure shows that the numerical model does relatively well at predicting peak floor displacement response. The model appears conservative in all cases except the NS direction for the MCE_R-01 test.

Fig. 11 shows the absolute value of the peak roof drift ratio from the numerical results versus the experimental results calculated from the accelerometer data. The accelerometer data are used in lieu of the direct displacement measurements due to greater confidence in that experimental data, as previously described. A 1:1 diagonal line is shown, representing a perfect correlation between numerical and experimental results. Additionally, a shaded error band showing $+/-0.25\%$ peak roof drift is also included. The figure shows that, on average, the numerical model predicts peak roof drift ratio response with good accuracy. In the north-south direction, the numerical model slightly overpredicts peak roof drift ratio response, again likely due to the contribution of the stairs and gravity framing captured in the east-west direction. In the east-west shaking direction, only one ground motion falls outside the 0.25% drift error band, and no tests fall outside the band in the north-south direction.

J. Struct. Eng., 2025, 151(11): 04025180

This work is made available under the terms of the Creative Commons Attribution 4.0 International license.

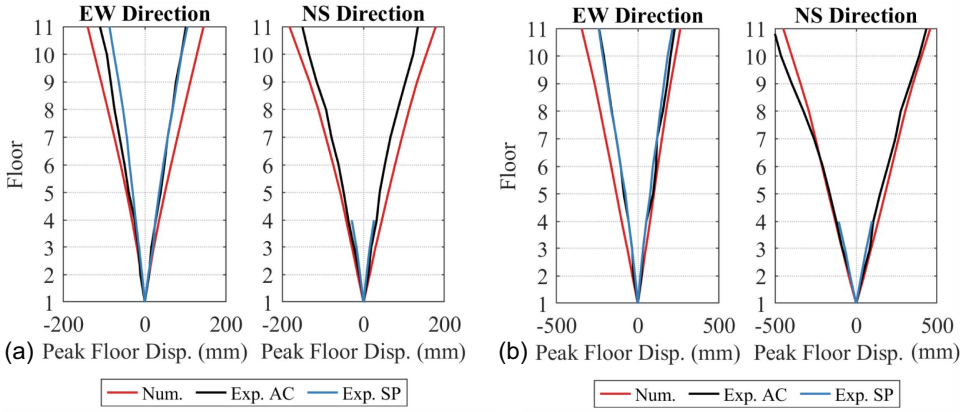

Fig. 10. Experimental and numerical peak floor displacement comparisons for test ID: (a) 225-07; and (b) MCE_R-01.

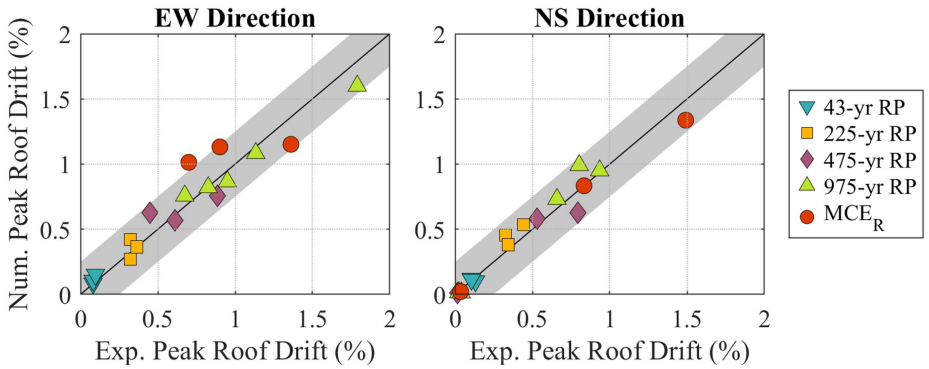

Fig. 11. Summary comparison of numerical and experimental peak roof drifts.

Experimental and numerical results were also compared in terms of interstory drift ratios (ISD). Similar to floor displacement comparisons, experimental results were computed using double-integrated accelerometers on each floor and the diagonal string potentiometers. Fig. 12 shows ISD time history experimental and numerical comparisons for test ID 225-07 and MEC_R-01. Fig. 12 shows that the two methods for calculating ISD do not produce results that are as similar as when comparing floor displacements. At lower hazard levels, the ISD time history results calculated from the accelerations show some large oscillations towards the end of the record. This behavior is likely erroneous because it does not match in-person visual observations or results calculated from the string potentiometers. Results calculated from the accelerations could be improved through more sophisticated filtering and baseline correction processes. Overall, peak ISD values agree well between the instruments. Like floor displacement comparisons, at low hazards, the results calculated from the string potentiometers are smaller than the accelerometer results. However, at smaller hazards, all measured displacements are very small. At larger hazard levels [e.g., Fig. 12(b)], the ISD values calculated from the accelerometer data and the string potentiometer data are more similar.

In general, the numerical model was able to predict the time history of the ISD response relatively well. Similar to the floor displacement discussion, the numerical model seems to slightly overpredict response in the east-west direction and underpredict response in the north-south direction. This discrepancy is likely because the numerical model does not include the stair system and gravity framing contributions that are more prominent in the east-west shaking direction. Additionally, ISD is somewhat overpredicted by the model for the lower hazard level.

Peak ISD profile comparisons are shown in Fig. 13. In the north-south direction, peak values calculated from the string potentiometer data were not computed for Stories 4 and 5 due to the missing instruments. In the plots, a dashed line is added between Stories 3 and 6 results to extrapolate a prediction of what likely occurred. In these plots, the numerical results show a much smoother response up the height of the building. Both experimental methods (but particularly the accelerometer calculation method) show the ISD profile up the height of the building to be more jagged. Note that the peak drift at all stories does not necessarily occur at the same time step in either the numerical or experimental results which can certainly result in nonsmooth peak drift profiles. However, some of the kinks in the profiles are likely a result of slight errors in the experimental data and processing that magnify when drifts are computed using the relative measurements between floors. While some of the smaller kinks could be real building response, the larger kinks would indicate that the walls underwent extreme curvature changes between stories. Most likely, this did not happen because the rocking walls were continuous, and no damage was observed during testing. Overall, these results show that the numerical model can predict peak ISD values.

Peak ISD response of the building is summarized in Fig. 14, which plots numerical peak ISDs versus experimental peak ISDs, calculated from the string potentiometer data. A 1:1 diagonal correlation line and a $+/-0.25\%$ peak ISD error band are again shown. Results show that the numerical model predicts peak ISD response well. Similar to peak roof displacements, the numerical model slightly overpredicts response in the north-south direction, likely due to the contribution of the stairs and gravity framing captured in the east-west direction. In both directions, two ground

This work is made available under the terms of the Creative Commons Attribution 4.0 International license.

This work is made available under the terms of the Creative Commons Attribution 4.0 International license.

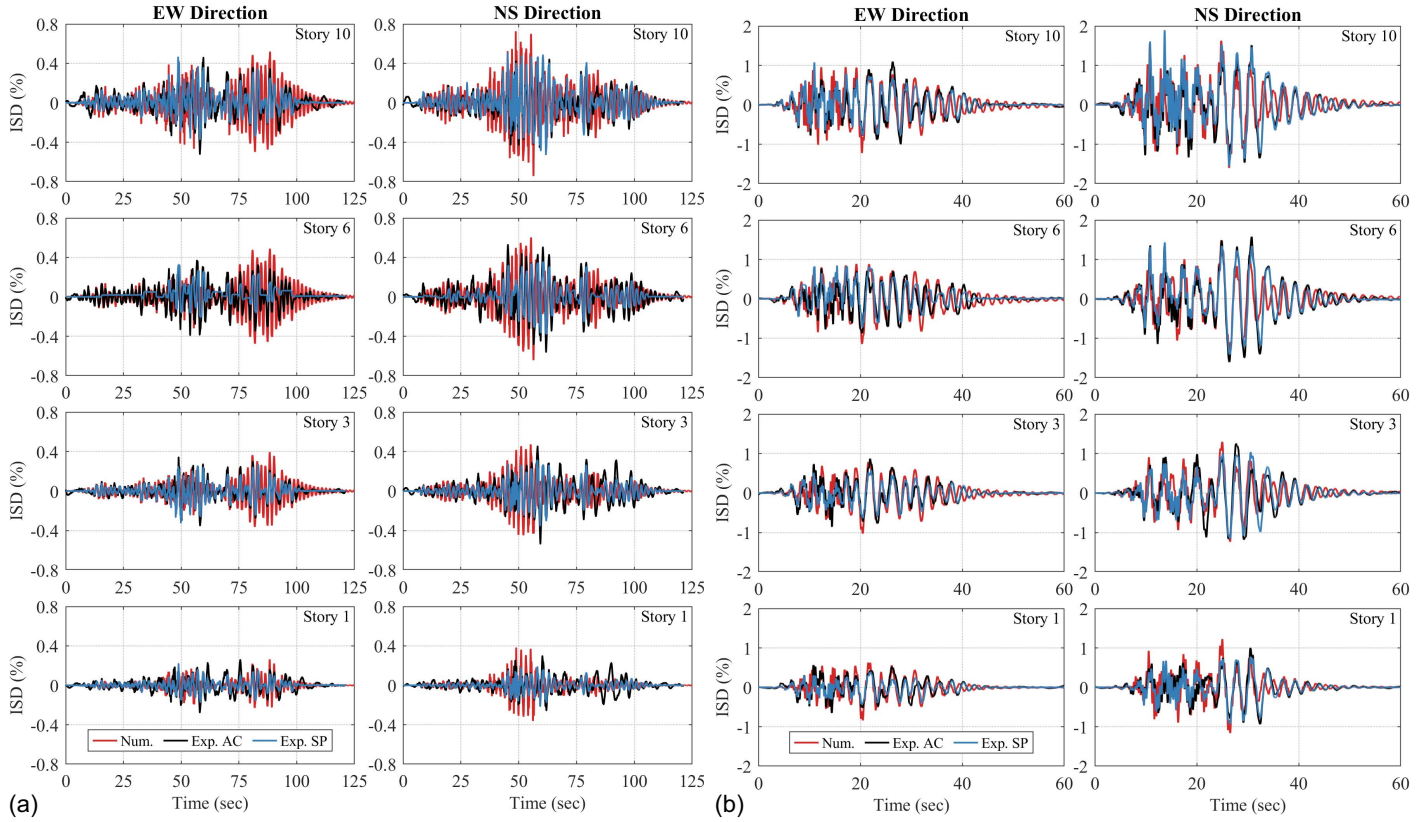

Fig. 12. Experimental and numerical ISD ratio time history comparisons for test ID: (a) 225-07; and (b) MCE_R-01.

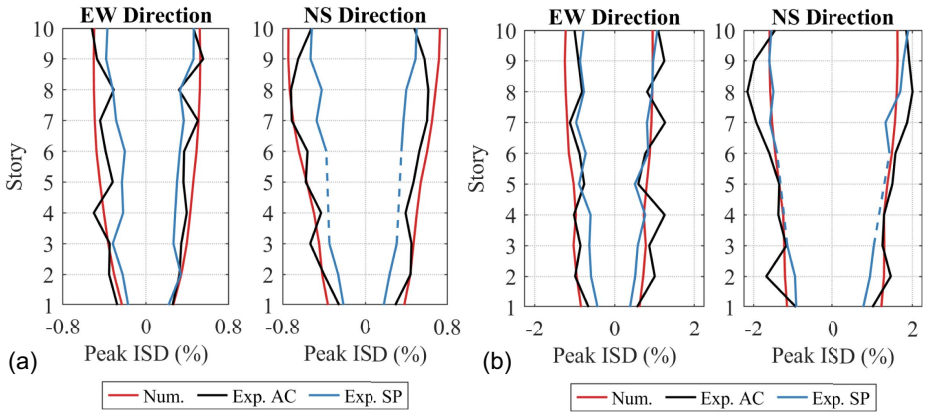

Fig. 13. Experimental and numerical peak ISD comparisons for test ID: (a) 225-07; and (b) MCE_R-01.

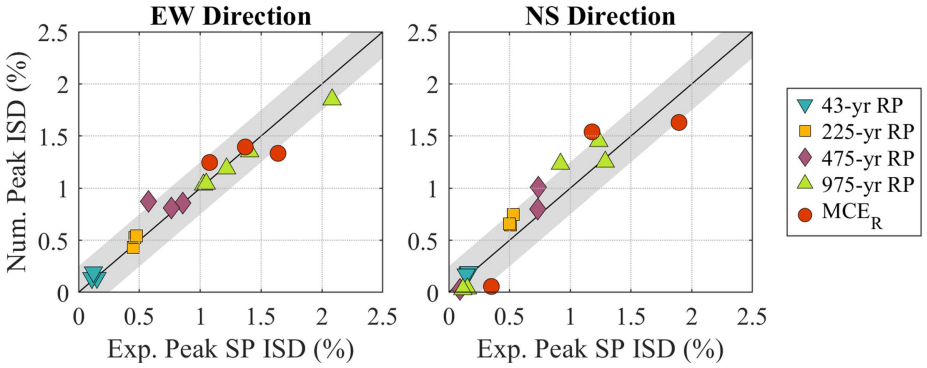

Fig. 14. Summary comparison of numerical and experimental peak ISDs calculated from string potentiometer data.

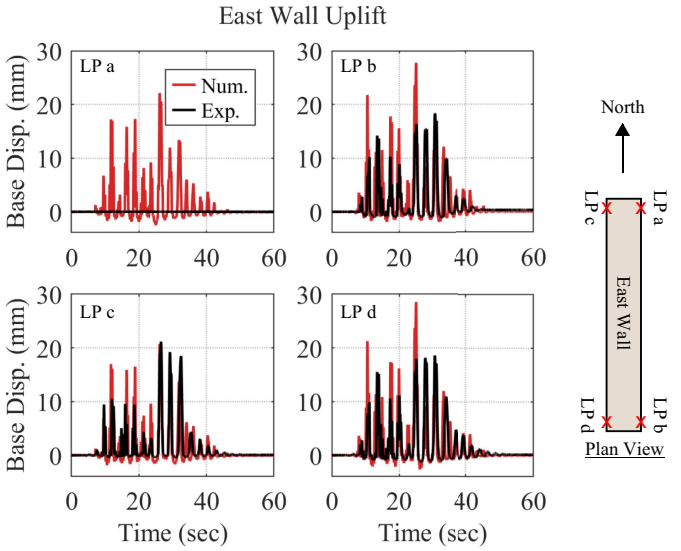

Fig. 15. Experimental and numerical results comparison of the east wall base displacement (disp.) for test ID MCE_R-01.

motions fall outside the 0.25% peak ISD error band but are just outside the band. As shown, the model is accurate but generally conservative in terms of predicting peak ISD, making it useful for design.

Experimental and numerical results were also compared by studying rocking wall uplift and compression deformations at the wall base rocking interfaces. For this comparison, experimental results were taken from unfiltered recordings of vertically orientated linear potentiometers located near the four corners of each wall panel. On one end, the linear potentiometers were anchored to the fixed foundation, and on the other, they were anchored to the wall panel. For the numerical results, output from the zero-length multispring located closest to the corresponding linear potentiometer location was used. Fig. 15 shows these results for the east wall from test ID MCE_R-01 (negligible uplift occurred in test ID 225-07). The plan view graphic in the figure can be referenced to show the approximate locations of the linear potentiometers (LP) plotted for the east wall. No experimental data are shown for LP due to an error in instrument data collection during testing. This figure shows that the numerical model can capture and predict the general uplift behavior. However, it tends to overpredict the peak values of both uplift and compressive deformation. Although not shown explicitly, this trend was particularly true for smaller hazard level tests. This indicates that the multispring element utilized in the OpenSees model can model uplift well to predict overall building performance, but additional revision of parameters such as strain penetration length and the mass timber stress–strain relationship could be revised to achieve a more accurate model of the localized behavior at the base of the walls. This is consistent with visual performance assessment; damage to the base of the wall panels is predicted in the OpenSees model with some moderate splitting predicted at the large hazard levels, but negligible damage was observed during testing.

Figs. 16 and 17 compare numerical and experimental results for peak wall base uplift (with a $+/-5$ mm error band) and peak compressive deformation values (with a $+/-1$ mm error band), respectively. Results in these plots show the overall peak value for each wall. In general, the numerical model overpredicted uplift. For the east and south walls, only two tests fall outside the error band. For the north and west walls, four and five tests fall outside the error band, respectively. For peak wall base compressive deformations, the numerical model slightly underpredicted experimental results on the north and south CLT walls. For the east and west MPP walls, the numerical model slightly overpredicted experimental results. For the north, south, east, and west walls, only four, two, two, and five tests fell outside the error band. Overall, model predictions for uplift and compressive deformation are in reasonably good agreement with the experimental results.

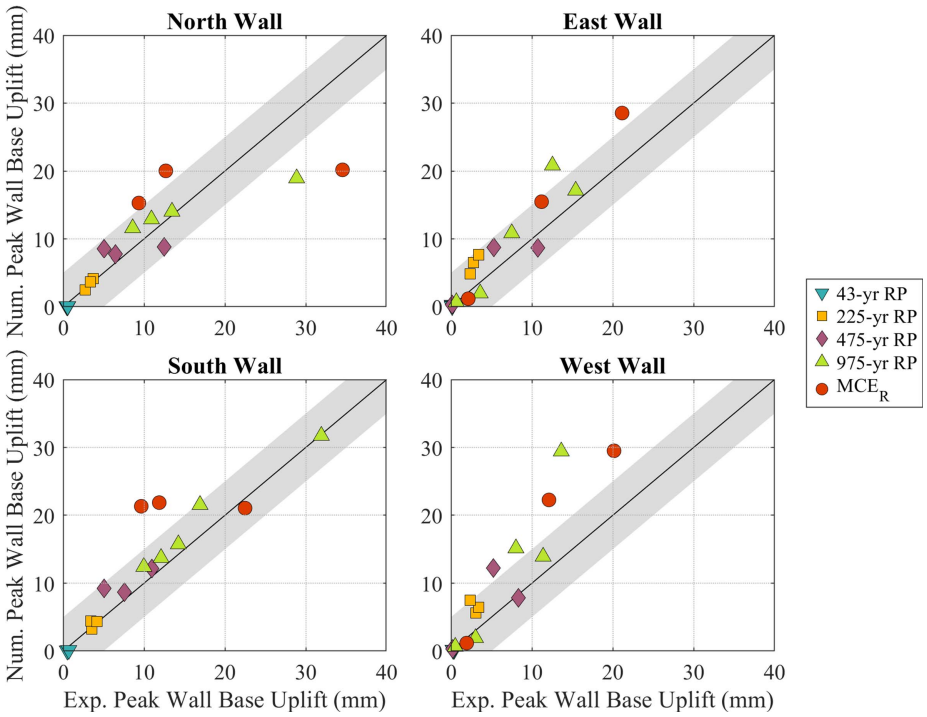

Fig. 16. Summary of experimental and numerical peak wall base uplift.

This work is made available under the terms of the Creative Commons Attribution 4.0 International license.

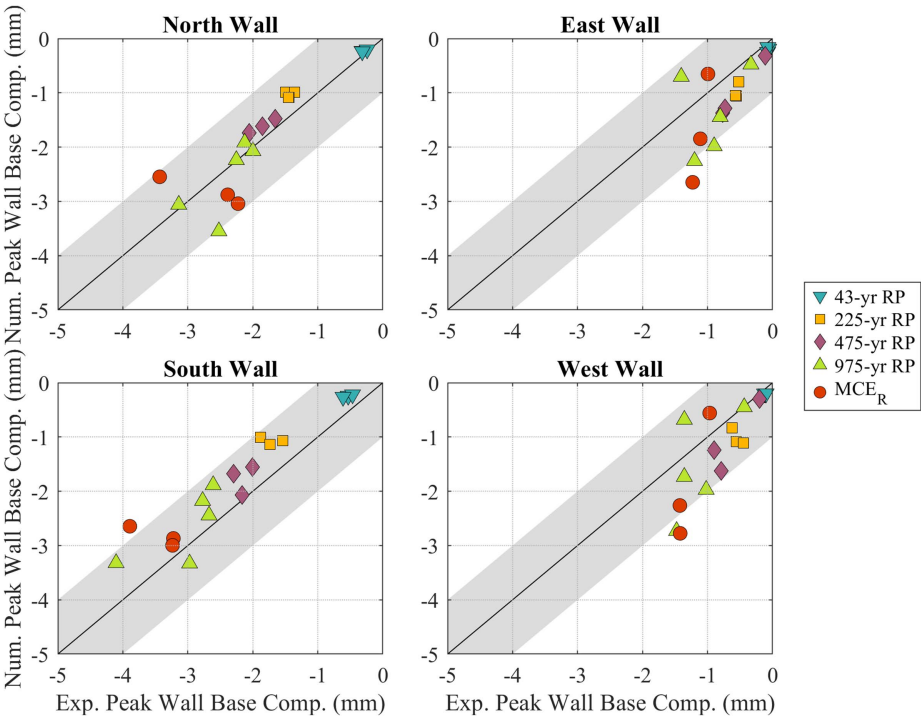

Fig. 17. Summary of experimental and numerical peak wall base compression deformations.

Summary and Conclusions

A 3D nonlinear numerical model was developed in OpenSees for design and lateral performance prediction of the NHERI TallWood 10-story specimen tested on the NHERI LHPOST facilities. The fully mass timber building had four PT mass timber rocking walls as the lateral force-resisting system. The building, designed for Seattle, WA, USA, was tested dynamically under suites of ground motions ranging in hazard level from 43-year return period events to motions representing MCE_R.

The presented 3D numerical model was used for the PBD design and building response prediction. The model includes a detailed representation of the PT rocking wall lateral force-resisting system. Base rocking and inelastic deformations in the wall panels are modeled using a newly developed 3D multispring element that captures in-plane and out-of-plane wall rocking. The element consists of compression-only parallel springs distributed along the base of the wall panel to model uplift and compressive deformation. A Rayleigh damping model is recommended with the first and second damping coefficients calculated using damping ratios of 0.05 and 0.06 and periods corresponding to the rocking mode period and a period that captures at least 90% mass participation, respectively. For the calculation of the first damping coefficient, it is recommended that a longer period, representative of the base rocking period, is used over the first mode from modal analysis to avoid overdamping the base rocking modes that contribute significantly to the overall behavior, particularly for higher intensity ground motions.

Comparisons of experimental and numerical results show that the presented modeling methodology can predict building response at both global and local levels. Floor displacements and ISD ratios (global level) match well between experimental and numerical results for both time history responses and peak values. Wall base uplift and compressive deformations (local level) between experimental and numerical results also match well for the shape of the time history response and moderately well for peak response values. Peak values of wall base uplift and compressive deformations could likely be improved through modifications to the constitutive model for the wall panel bases or the assumed strain penetration length.

This paper provides confidence that future projects that aim to use PT mass timber rocking walls in tall buildings can use a robust nonlinear modeling method to reliably predict seismic performance. The presented 3D distributed multispring element captures uplift and compression demands, providing designers and researchers with a reliable modeling method for capturing both in-plane and out-of-plane rocking. This paper also demonstrates that modern approaches for PBD design can be applied to tall timber buildings and result in behavior that matches design intents.

Recommendations for Future Research

Studying the effects of unintentional shake table movement in the three rotational DOFs was outside the scope of this work. For this study, the recorded rotations were neglected. However, even minor rotations of the shake table platen may affect the results. Investigating the effects of unintentional but recorded table platen rotation is recommended. Additionally, data studying the behavior of mass timber materials under large stress gradients and combined stress, such as in the compression zone at the rocking wall toe, are lacking. In these locations, the material is under large compression and shear, but both pass through only the portion of the wall that is in contact with the foundation. This results in large local stress that then distributes through the rest of the wall with increasing height above the base. In numerical system models needed for engineering design such as the one used here, uniaxial material models are necessary and are calibrated based on laboratory tests of mass timber under uniform compression, which neglects any effects of combined shear and compression stress and the likely beneficial effect for the compression stress distributing to larger sections of the walls with increasing height above the base. There is room for improvement in

This work is made available under the terms of the Creative Commons Attribution 4.0 International license.

both the laboratory tests used to establish the material properties for the compression zones of mass timber rocking walls and in the development of uniaxial material models from those tests.

Data Availability Statement

Some or all data, models, or code generated or used during the study are available in a repository online in accordance with funder data retention policies.

Acknowledgments

Financial support for this study was provided by the National Science Foundation through Grants CMMI 1635227, 1634628, 1636164, and 1634204. Any opinions, findings, conclusions, and recommendations presented in this paper are those of the authors and do not necessarily reflect the views of the sponsors. The Revit model used for the construction of the NHERI TallWood 10-story specimen was provided by Aleesha Busch.

Author Contributions

Sarah Wichman: Conceptualization; Data curation; Formal analysis; Investigation; Methodology; Visualization; Writing – original draft; Writing – review and editing. Jeffrey W. Berman: Conceptualization; Funding acquisition; Investigation; Methodology; Project administration; Supervision; Writing – review and editing. Reid B. Zimmerman: Conceptualization; Data curation; Funding acquisition; Supervision; Writing – review and editing. Shiling Pei: Conceptualization; Data curation; Funding acquisition; Supervision; Writing – review and editing.

References

Akbas, T., R. Sause, J. M. Ricles, R. Ganey, J. Berman, S. Loftus, J. D. Dolan, S. Pei, J. W. van de Lindt, and H.-E. Blomgren. 2017. "Analytical and experimental lateral-load response of self-centering posttensioned CLT walls." *J. Struct. Eng.* 143 (6): 04017019. https://doi.org/10.1061/(ASCE)ST.1943-541X.0001733.

Ancheta, T. D., et al. 2014. "NGA-west2 database." *Earthquake Spectra* 30 (3): 989–1005. https://doi.org/10.1193/070913EQS197M.

APA (APA—Then Engineered Wood Association). 2021. *APA product report PR-1325 Freres mass ply panels (MPP) and mass ply lams (MPL) beams and columns*. Rep. No. PR-L325. Lyons, CO: APA.

ASCE. 2016. *Minimum design loads for buildings and other structures*. ASCE 7-16. Reston, VA: ASCE.

AWC (American Wood Council). 2018. *National design specification for wood construction*. Leesburg, VA: AWC.

Baird, A., T. Smith, A. Palermo, and S. Pampanin. 2014. "Experimental and numerical study of U-shape flexural plate (UFP) dissipaters." In *Proc., New Zealand Society for Earthquake Engineering 2014 Technical Conf. and AGM*. Auckland, New Zealand: New Zealand Society for Earthquake Engineering.

Barbosa, A. R., L. G. Rodrigues, A. Sinha, C. Higgins, R. B. Zimmerman, S. Breneman, S. Pei, J. W. van de Lindt, J. Berman, and E. McDonnell. 2021. "Shake-table experimental testing and performance of topped and untopped cross-laminated timber diaphragms." *J. Struct. Eng.* 147 (4): 04021011. https://doi.org/10.1061/(ASCE)ST.1943-541X.0002914.

Brown, J. R., M. Li, A. Palermo, S. Pampanin, and F. Sarti. 2021. "Experimental testing of a low-damage post-tensioned c-shaped CLT core-wall." *J. Struct. Eng.* 147 (3): 04020357. https://doi.org/10.1061/(ASCE)ST.1943-541X.0002926.

Busch, A., R. B. Zimmerman, S. Pei, E. McDonnell, P. Line, and D. Huang. 2022. "Prescriptive seismic design procedure for post-tensioned mass timber rocking walls." *J. Struct. Eng.* 148 (3): 04021289. https://doi.org/10.1061/(ASCE)ST.1943-541X.0003240.

Ganey, R. 2015. "Seismic design and testing of rocking cross laminated timber walls." M.S. thesis, Dept. of Civil and Environmental Engineering, Univ. of Washington.

Ganey, R., J. Berman, T. Akbaş, S. Loftus, J. Daniel Dolan, R. Sause, J. Ricles, S. Pei, J. V. D. Lindt, and H. E. Blomgren. 2017. "Experimental investigation of self-centering cross-laminated timber walls." *J. Struct. Eng.* 143 (10): 04017135. https://doi.org/10.1061/(asce)st.1943-541x.0001877.

Huang, D. 2023. "Optimized seismic design and dynamic response analysis of mass timber rocking wall lateral system." Ph.D. thesis, Dept. of Civil and Environmental Engineering, Colorado School of Mines.

Iqbal, A., S. Pampanin, A. Palermo, and A. H. Buchanan. 2015. "Performance and design of LVL walls coupled with UFP dissipaters." *J. Earthquake Eng.* 19 (3): 383–409. https://doi.org/10.1080/13632469.2014.987406.

Kelly, J. M., R. I. Skiner, and A. J. Heine. 1972. "Mechanisms of energy absorption in special devices for use in earthquake resistant structures." *Bull. N.Z. Soc. Earthquake Eng.* 5 (3): 63–88. https://doi.org/10.5459/bnzsee.5.3.63-88.

Kovacs, M. 2016. "Design of controlled rocking heavy timber walls for low-to-moderate seismic hazard regions." M.S. thesis, Dept. of Civil Engineering, McMaster Univ.

Kurama, Y., S. Pessiki, R. Sause, and L. Lu. 1999. "Seismic behavior and design of unbonded post-tensioned precast concrete walls." *PCI J.* 44 (3): 72–89. https://doi.org/10.15554/pcij.05011999.72.89.

LATBSDC (Los Angeles Tall Buildings Structural Design Council). 2014. *An alternative procedure for seismic analysis and design of tall buildings located in the Los Angeles region*. Los Angeles: Los Angeles Tall Buildings Structural Design Council.

Mazzoni, S., T. Kishida, V. Contreras, S. K. Ahdi, D. Y. Kwak, Y. Bozorgnia, and J. P. Stewart. 2021. *NGA-sub flatfile: R211022*. Los Angeles: The B. John Garrick Institute for the Risk Sciences. https://doi.org/10.34948/N3Z59T.

McKenna, F., M. H. Scott, and G. L. Fenves. 2010. "Nonlinear finite-element analysis software architecture using object composition." *J. Comput. Civ. Eng.* 24 (1): 95–107. https://doi.org/10.1061/(ASCE)CP.1943-5487.0000002.

Newcombe, M. P. 2015. "The connection response of rocking timber walls." *N.Z. Timber Des.* 23 (1): 21–28.

Newcombe, M. P., S. Pampanin, A. Buchanan, and A. Palermo. 2008. "Section analysis and cyclic behavior of post-tensioned jointed ductile connections for multi-story timber buildings." Supplement, *J. Earthquake Eng.* 12 (S1): 83–110. https://doi.org/10.1080/13632460801925632.

NIED (National Research Institute for Earth Science and Disaster Resilience). 2018. "Strong-motion seismograph networks (k-net, kik-net)" Accessed October 11, 2020. https://www.kyoshin.bosai.go.jp/kyoshin/docs/overview_kyoshin_index_en.html.

Palermo, A., S. Pampanin, and A. Buchanan. 2006. "Experimental investigation on LVL seismic resistant wall and frame subassemblies." In *Proc., First European Conf. on Earthquake Engineering and Seismology*. Istanbul, Turkey: European Association for Earthquake Engineering.

Palermo, A., S. Pampanin, and A. Carr. 2005. *Efficiency of simplified alternative modeling approaches to predict the seismic response of precast concrete hybrid systems*. Christchurch, New Zealand: Univ. of Canterbury.

Pampanin, S., M. J. N. Priestley, and S. Sritharan. 2001. "Analytical modeling of the seismic behavior of precast concrete frames designed with ductile connections." *J. Earthquake Eng.* 5 (3): 329–367. https://doi.org/10.1142/S1363246901000467.

PEER (Pacific Earthquake Engineering Research Center). 2017. *Guidelines for performance-based seismic design of tall buildings*. Berkeley, CA: PEER.

Pei, S., et al. 2024a. "Shake table test of a resilient full-scale ten-story mass timber building." In *Shake table test of a resilient full-scale ten-story mass timber building*. West Lafayette, IN: DesignSafe-CI. https://doi.org/10.17603/ds2-sxq1-p731.

This work is made available under the terms of the Creative Commons Attribution 4.0 International license.

Pei, S., et al. 2024b. "Shake table testing of a full-scale ten-story resilient mass timber building." *J. Struct. Eng.* 150 (12): 04024183. https://doi.org/10.1061/JSENDH.STENG-13752.

Pei, S., J. W. van de Lindt, A. R. Barbosa, J. W. Berman, E. McDonnell, J. D. Dolan, H.-E. Blomgren, R. B. Zimmerman, D. Huang, and S. Wichman. 2019. "Experimental seismic response of a resilient 2-story mass-timber building with post-tensioned rocking walls." *J. Struct. Eng.* 145 (11): 04019120. https://doi.org/10.1061/(ASCE)ST.1943-541X.0002382.

Priestley, N. 1991. "Overview of press research program." *PCI J.* 36 (4): 50–57. https://doi.org/10.15554/pcij.07011991.50.57.

Rodrigues, L. G., et al. 2024. "Analytical and numerical models for wind and seismic design and assessment of mass timber diaphragms." *J. Struct. Eng.* 150 (2): 04023229. https://doi.org/10.1061/JSENDH.STENG-12265.

Sarti, F. 2015. "Seismic design of low-damage post-tensioned timber wall systems." Ph.D. thesis, Dept. of Civil and Environmental Engineering, Univ. of Canterbury.

Soti, R., T. X. Ho, and A. Sinha. 2021. "Structural performance characterization of mass plywood panels." *J. Mater. Civ. Eng.* 33 (10): 04021275. https://doi.org/10.1061/(asce)mt.1943-5533.0003902.

Spieth, H. A., A. J. Carr, S. Pampanin, A. G. Murahidy, and J. Mander. 2004. *Modeling of precast prestressed concrete from structures with rocking beam-column connections*. Rep. No. 2004-01, Christchurch, New Zealand: Univ. of Canterbury.

Wichman, S. 2018. "Large-scale dynamic testing of rocking cross laminated timber walls." M.S. thesis, Dept. of Civil and Environmental Engineering, Univ. of Washington.

Wichman, S. 2023. "Seismic behavior of tall rocking mass timber walls." Ph.D. thesis, Dept. of Civil and Environmental Engineering, Univ. of Washington.

Wichman, S., J. W. Berman, and S. Pei. 2022. "Experimental investigation and numerical modeling of rocking cross laminated timber walls on a flexible foundation." *Earthquake Eng. Struct. Dyn.* 51 (7): 1697–1717. https://doi.org/10.1002/eqe.3634.

WoodWorks. 2023. *CLT diaphragm design guide*. Washington, DC: WoodWorks—Wood Products Council.

Wright, D. 2023. "Vertical vibration of mass timber floors subjected to seismic and footfall loading." M.S. thesis, Dept. of Civil and Environmental Engineering, Univ. of Washington.

Zimmerman, R. B., and E. McDonnell. 2018a. "Framework—Innovation in re-centering mass timber wall buildings." In *Proc., Eleventh US National Conf. on Earthquake Engineering*. Oakland, CA: Earthquake Engineering Research Institute.

Zimmerman, R. B., and E. McDonnell. 2018b. "Recommended language for mass timber wall buildings in the LATBSDC an alternative procedure for seismic analysis and design of tall buildings located in the Los Angeles region." In *Proc., Los Angeles Tall Building Structural Design Council Conf.* Los Angeles: Los Angeles Tall Building Structural Design Council.

This work is made available under the terms of the Creative Commons Attribution 4.0 International license.